Structural investigation of single-source evaporation of phase pure CsFAPbI₃ and FAPbI₃ perovskite thin films

Nadja Klipfel [1], Muhammed P U Haris[2], Samrana Kazim[2,5], Albertus Adrian Sutanto[1], Naoyuki Shibayama[3], Hiroyuki Kanda[1], Abdullah M. Asiri,[4] Cristina Momblona[1*], Shahzada Ahmad[2,5*], Mohammad Khaja Nazeeruddin[1,6*]

[1]*Group for Molecular Engineering of Functional Materials, Institute of Chemical Sciences and Engineering, École Polytechnique Fédérale de Lausanne, Valais Wallis, Rue de l'Industrie 17, 1950 Sion, Switzerland.*

[2]*BCMaterials, Basque Center for Materials, Applications, and Nanostructures, UPV/EHU Science Park, Leioa, 48940 Spain.*

[3]Department of Biomedical Engineering, Toin University of Yokohama, 1614 Kurogane, Aoba, Yokohama, Japan.

[4]Center of Excellence for Advanced Materials Research (CEAMR), King Abdulaziz University, P.O. Box 80203, 21589 Jeddah, Saudi Arabia.

[5]IKERBASQUE, Basque Foundation for Science, Bilbao 48009, Spain.

[6]Department of Materials Science and Engineering, City University of Hong Kong, Kowloon, Hong Kong.

Abstract

Thermal vacuum deposition is a stimulating technique for upscaling perovskite solar cells. The operational complexity of multi-source vapor deposition (MSVD) in achieving stoichiometric perovskite layers may impede its implementation. The single-source vapor deposition (SSVD) method has recently emerged as an alternative for MSVD due to its inherent functionality. Here for the first time, we demonstrate the successful SSVD approach in fabricating pure $CsFAPbI_3$ and $FAPbI_3$ thin films from pre-synthesized perovskite powders. A series of structural, optoelectronic, and morphological investigations were carried out to optimize the phase purity and shelf-life of the deposited thin films. Furthermore, we probed the perovskite layer compatibility with various underlayers; we noted the organic underlayer displayed superiority over the metal oxide layer, suggesting the suitability of *p-i-n* devices over the *n-i-p*.

1 Introduction

The power conversion efficiency (PCE) of perovskite solar cells (PSCs) improved over the last decade, from 3.8% in 2009 to over 25% today.[1,2] This increase in efficiency is remarkable and makes perovskite solar cells a promising technology toward reducing carbon emissions.[3] Perovskites are considered inexpensive,[4] easy to process, and recyclable,[5] factors contributing to achieving sustainability goals.[6] Nevertheless, commercialization is still challenging due to the instability of the overall device and the perovskite's material intolerance to environmental stresses[7–10], complicating large-scale production. Various strategies such as compositional and process engineering have been adopted to overcome these difficulties. The degradation-prone methylammonium lead triiodide ($MAPbI_3$) was replaced by formamidinium lead triiodide ($FAPbI_3$) due to its reduced optical bandgap and higher thermal stability.[11] However, the critical phase transition (α- to δ-phase) of $FAPbI_3$ at room temperature hindered its application. Further extension of compositional engineering using the FA-site doping with smaller cations and anions such as methylammonium (MA^+), cesium (Cs^+), bromine (Br^-), chloride (Cl^-) helped to stabilize the perovskite phase.[12,13] Through process engineering, various thin film fabrication methods such as the two-step sequential spin-coating method, a one-step spin-coating method, a vapor-assisted solution process, and the vacuum deposition method emerged. While solution-processed PSCs possess low-cost and higher efficiencies at the lab scale, the technique is not yet fully optimized for large-scale PSCs fabrication.[14–16] Moreover, toxic organic solvents are used in perovskite precursor solutions. Employing these at an industrial scale could severely impact human health and the environment. [17,18] In this

context, vacuum deposition techniques provide a solvent-free alternative to solution processing. Advantages include large-scale compatibility, nanometer-scale precision, and prevention of intermixing of different layers.[19,20]

In conventional vacuum deposition methods (also known as multi-source vacuum deposition (MSVD)), precursor powders are sublimed simultaneously from different crucibles. [14] In literature, MSVD was first was reported by Borchert *et al.* in 2017, describing the large-area (16 cm^2) fabrication of FAPbI$_3$ films with a stabilized efficiency of 14.2% [20] Inspired by solution-process techniques, MAI,[21] Cs^{+}[22], PbBr$_2$[23], and excess FAI were co-sublimed to stabilize the α-FAPbI$_3$ layer, leading to two-, three- or four-source vacuum deposition processes.[24] Controlling the stoichiometric ratio in MSVD-fabricated thin films is difficult for mixed anion or mixed cation perovskites. Each material must be calibrated first and later in the perovskite to obtain the correct stoichiometry. Evaporating, therefore, a pre-synthesized perovskite material from a single source could shorten the effort in the evaporation processes and could be interesting for commercial application.

Moreover, high vapor pressure and low decomposition temperatures of organic ammonium halides challenge compositional tuning of the final thin film.[25] Single-source vapor deposition technique (SSVD), where the pre-synthesized perovskite powder is sublimed instead of individual precursors, has emerged as one possible solution to overcome such barriers. Fan *et al.* was the first to report the SSVD for halide perovskite thin films and deposited a 400 nm thick MAPbI$_3$ layer leading to a 10% PCE.[16] Later, Ajjouri *et al.* fabricated inorganic CsPbX$_3$ thin films employing SSVD. They observed that their thin films showed better crystallinity relative to MSVD.[26] It was suggested that during SSVD, at least a portion of perovskite powder gets sublimed in the form of CsPbX$_3$ instead of undergoing a complete decomposition to CsX+PbX$_2$ as observed for the MSVD process. The quick and straightforward operational procedure made SSVD superior over MSVD. Recently, Crane *et al.* employed the SSVD technique for the ball-milled (FA$_{0.81}$MA$_{0.14}$Cs$_{0.05}$) Pb(Cl$_{0.02}$Br$_{0.14}$I$_{0.84}$)$_3$ perovskite powder observing PbI$_2$ excess in the deposited film. Excess use of FAI and MABr in the ball-milled powder led to proper perovskite formation.[25] The presence of unreacted and excess precursor materials could impeds the batch-to-batch reproducibility of perovskite powder and thin film stoichiometries.

Thus, the simplification of the vacuum deposition technique is paramount, especially when considering the up-scaling of this future technology. Herein, we have successfully employed

the SSVD technique to fabricate CsFAPbI$_3$ and FAPbI$_3$ thin films from pre-synthesized perovskite powders for the first time. We synthesized the perovskite powders without excess of the precursors to investigate if stoichiometric thin films can be evaporated from stoichiometry perovskite powders. The structural and optoelectronic studies confirmed the phase-pure thin films with commendable stability, and the perovskite layer compatibility with different underlayers was studied.

2. Results

2.1 Synthesis and analysis of pre-synthesized powders

The α-CsFAPbI$_3$ and δ-FAPbI$_3$ powders (we termed CsFAPbI$_3$ powder and FAPbI$_3$ powder) were synthesized and detailed in the experimental section (Supporting Figure S1). The FAPbI$_3$ powder was synthesized accordingly,[27] while the CsFAPbI$_3$ powder was synthesized by simply heating the previously reported δ-CsFAPbI$_3$ at 150 °C for 1 hour in a tube furnace.[27] We characterized the perovskite powders using X-ray photon spectroscopy (XPS), powder X-ray diffraction (PXRD), thermogravimetric (TGA) analyses. XPS was used to analyze the elemental composition and the nature of chemical bonding for both perovskite powders. The signals from the core levels are presented (Supporting Figure S2 for CsFAPbI$_3$ and Supporting Figure S3 for FAPbI$_3$). The XPS signals corresponding to Cs 3d$_{5/2}$ and Cs 3d$_{3/2}$ at 721.8 and 735.77 eV (Supporting Figure S2a), respectively, are visible for CsFAPbI$_3$ powder and a small shift in the I 3d$_{3/2}$= 615.38 eV I 3d$_{5/2}$= 626.88 eV (Supporting Figure S3b) and Pb 4f$_{7/2}$= 134.50 eV Pb 4f$_{5/2}$= 139.40 eV and (Supporting Figure S2c) core level signals emerges from the inclusion of the Cs.[27,28] The XPS signals for FAPbI$_3$ powder are I 3d$_{3/2}$= 615.75 eV I 3d$_{5/2}$= 627.25 eV, for I 3d and Pb 4f$_{7/2}$= 134.99 eV Pb 4f$_{5/2}$= 139.92 eV for Pb 4f, without any shift (Figure S3b and Figure S3c, respectively).[27] As depicted in the diffractograms (Supporting Figure S4), the powders exhibited exceptional phase purity with no trace of residual components.[27,29] The thermogravimetric (TGA) values were measured for the FAPbI$_3$ and CsFAPbI$_3$ powders (Supporting Figure S5). The FAPbI$_3$ is losing FAI at 325°C-397°C, and the CsFAPbI3 powder is losing FAI at 343°C-497°C. These findings and the low phase-transition temperature of both pre-synthesized perovskite powder suggested that solvent-free single-source evaporation is viable. This opened the pathway of replacing the complicated multi-source evaporation with single-source evaporation of pre-synthesized perovskite powders.
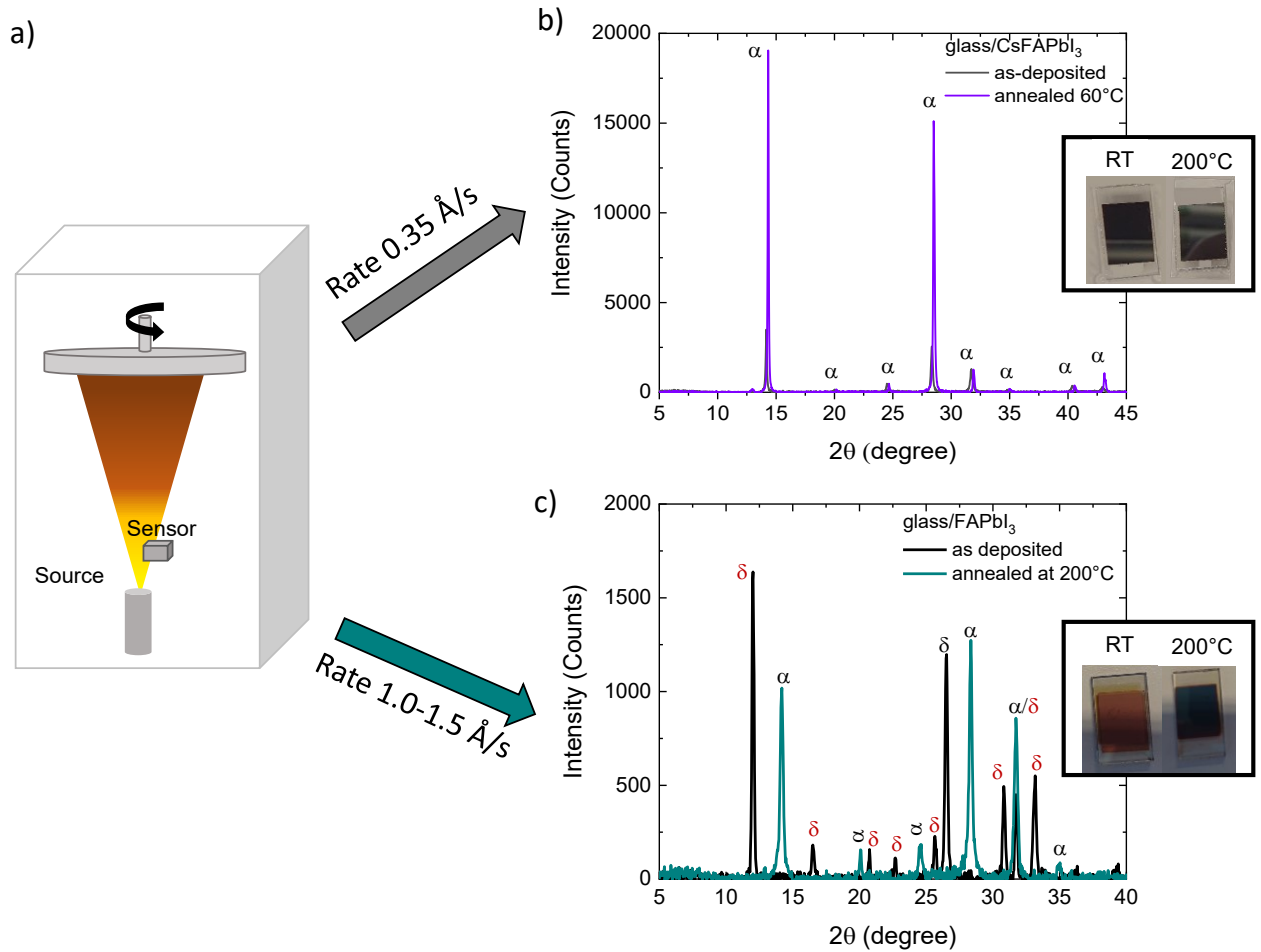
Figure 1. a) Schematic for single-source evaporation of pre-synthesized α-CsFAPbI$_3$ and δ-FAPbI$_3$ perovskite powder, b) PXRD diffractograms of CsFAPbI$_3$ thin films on the glass as-deposited and annealed, inset photographs of the films c), PXRD diffractograms of FAPbI$_3$ thin films on the glass as-deposited and annealed, inset photographs of the films.

2.1.1 PXRD, 2D-GIWAXS and photophysical characterization of single-source evaporated thin films

Figure 1a shows the schematic description of the single-source evaporation process used to sublime the perovskite powders. It is worth noting that, here, we have not used any precursor materials (like FAI or CsI) in excess as reported in the literature for mix-perovskites.[20] First, the thermal evaporation at subsequent evaporation rates was performed to optimize the thin film deposition process for the perovskite powders (Supporting Information, Table S1). The deposition rate is directly related to the sublimation power, i.e., the higher the rate, the higher the applied sublimation power. To simplify, we will describe the SSVD process by deposition rate in this paper. The CsFAPbI$_3$ powder was sublimed at three different deposition rates, i.e.,

0.25 Å/s, 0.35 Å/s, and 1.0-1.05 Å/s, and the phase purity of each deposited thin film were probed using PXRD measurements. As depicted in Figure S6, the diffractogram of the as-deposited CsFAPbI$_3$ at 0.35 Å/s reveals the characteristic α-phase diffractions, i.e., (100), (110), (111), (200), (210), (211), (220) and (300).[27] A faster deposition at 1.0-1.05 Å/s leads to δ-phase with two major reflexes at (022) and (211). Further, the slower deposition at 0.25 Å/s did lead to a mixed-phase perovskite where the collected diffractogram identified the presence of (100), (111), and (211) reflections indicating the α-phase along with the (022) and (211) reflections indicating the δ-phase. Similarly, the FAPbI$_3$ powder was sublimed at two different rates, i.e., 1.0 −1.05 Å/s and 3.0 −3.05 Å/s. At 1.0 −1.05 Å/s deposition, diffractograms indexed with (010), (011), (120), (022), (012), (021), (122), (130), (022) and (204) reflections indicating the δ-phase. Whereas deposition at 3.0−3.05 Å/s lead to a mixed-phase perovskite layer which includes the α- and δ-phases along with excess PbI$_2$ (Supporting Figure S7a). We attribute the intense PbI$_2$ presence to the FAI decomposition at a faster deposition rate, which is in agreement with previous reports.[24] Further, we annealed, and diffractograms and UV-Vis absorption data were collected from all the thin films to probe the phase purity and crystallinity. CsFAPbI$_3$ deposited at 0.35 Å/s showed enhanced crystallinity through rapid annealing at 60 C for 5s (Supporting Figure S8). The reduced full width at half maximum (FWHM) (from for as-deposited 0.14° to annealed 0.11°) and enhanced peak intensity for (h00) planes indicate the improved crystallinity for annealed CsFAPbI$_3$ thin film (Supporting Figure S8). This is further substantiated by the enhanced UV-Vis absorption coefficient (Supporting Figure S9a), and the 0.35 Å/s deposition was identified as the optimum for CsFAPbI$_3$ powder. Similarly, the deposited FAPbI3 thin films were annealed at 200 °C, and from the corresponding diffractograms (Supporting Figure S7b) and the absorption data (Supporting Figure S9a) optimized the deposition rate as 1.0-1.05 Å/s.

We employed 2D grazing incidence wide-angle X-ray scattering (2D GIWAXS) at 0.12 °(**Figures 2a** and 2b) to track the crystal orientations in the optimized thin films. The integrated q-data analysis identified the presence of δ-CsFAPbI$_3$ in the as-deposited film (Figure 2c, q= 0.9 A^{-1}), which was not detected in PXRD. As depicted in Figure 2b, post-annealing at 60 °C resulted in a pure α-CsFAPbI$_3$ film. The azimuthal integration of the GIWAXS films at 100 reflexes (q=1.0 A^{-1}) showed a preferred crystal orientation along in-plane and out-of-plane at $\chi100 = 16°$ and $\chi100 = 79°$ (Figure S19a,b) for the unannealed film. , However, the post-annealing leads to a reordering of the film resulting in a less-preferred in- and out-of-plane orientation (Supporting Figure S9b, more flat part). From the

GIWAXS analysis for the post-annealed α-FAPbI$_3$ film (Supporting Figure S10), the q-integration of the image identified traces of δ-FAPbI$_3$ in the film (q= 0.8-0.9A^{-1}). The azimuthal integration of the GIWAXS 100 reflex (q = 1.0A^{-1}) shows a preferred crystal orientation with both in-and out-of-plane at $\chi 100 = 16°$ and $\chi 100 = 79°$, similar to the one described for the as-deposited CsFAPbI$_3$ film (Supporting Figure S10 a and S10 c). The collective analyses using Uv-Vis absorption, PXRD, and GIWAXS confirms the exceptional phase purity for CsFAPbI$_3$ and a commendable phase purity for FAPbI$_3$ thin films. Moreover, Figure S9a, 9b compares UV-Vis absorption spectra and the steady-state photoluminescence (PL) of α-CsFAPbI$_3$ and α-FAPbI$_3$ thin films. The blue-shifting of absorption onset and the red-shifting PL maximum (from 810 nm to 801 nm) indicates the inclusion of smaller Cs cations inclusion in the FAPbI$_3$ structure.[30] This certifies the applicability of our SSVD work in realizing mixed-perovskite thin films. We have carried out time-resolved photoluminescence (TRPL) measurements on the optimized CsFAPbI$_3$ and FAPbI$_3$ thin films, as shown in Supporting Figure S12. For the lifetime measurements, the samples were excited at 640 nm. The corresponding decays were fitted to a double exponential equation. The fast component (τ_1) is related to trap-assisted recombination at defect sites, and the slow component (τ_2) radiative recombination inside the grains.[31,32] As tabulated in Table S2, CsFAPbI$_3$ film exhibits τ_1 and τ_2 values of 18.89 ns and 61.61 ns, whereas FAPbI$_3$ thin film showed much longer lifetimes of 1.09 ns and 27.03 ns, respectively. These deposited SSVD thin films have short lifetimes than that of the solution-processed perovskites, which indicates trap-assisted recombination in the thin films.[33] However, the thin films from vapor deposition techniques typically display short lifetimes,[20,34] and optimization of the material properties in vapor deposition methods is required in the near future.
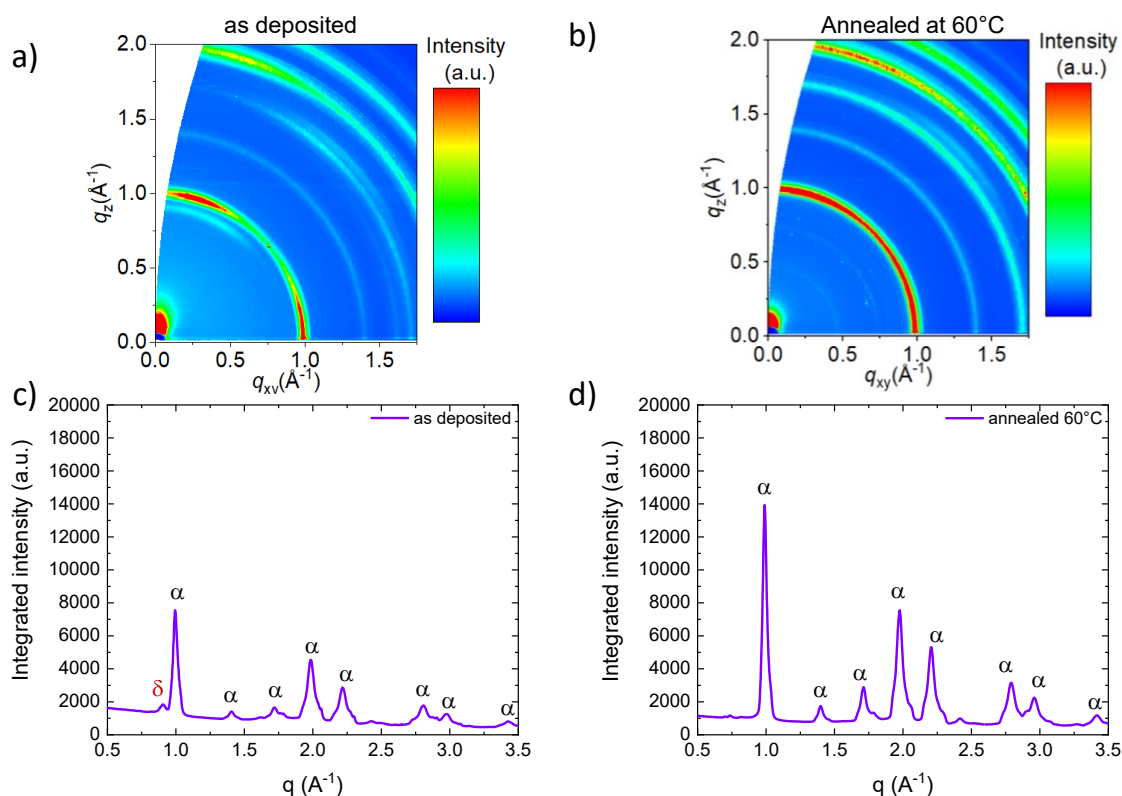
Figure 2: GIWAXS images taken at an angle of 0.12 of a) CsFAPbI₃ thin film as deposited b) CsFAPbI₃ film annealed at 60°C. Integrated q-data of the GIWAXS images for c) as-deposited CsFAPbI₃ film and d) CsFAPbI₃ film after post-annealing at 60°C.

2.1.2 Stability of thin films

The stability of fabricated perovskite layers is crucial for their implementations. The shelf-life of the CsFAPbI₃ (**Figure 3a**) and FAPbI₃ (Figure 3b) films on glass substrates were monitored by PXRD measurements over two weeks time. Contrary to the solution process method,[35,36] FAPbI₃ film showed superior storage or self-life stability than the CsFAPbI₃ film. Upon dry-air storage for 7 days, the CsFAPbI₃ layer showed a significant decrement in the (100) reflection intensity along with the emergence of new reflections belonging to the δ-phase (Figure 3a). Remarkably the annealed FAPbI₃ thin films did not show any sign of degradation within these two weeks, indicating superior film stability (Figure 3b). Further analysis is necessary for the unraveling of the underlying mechanisms.
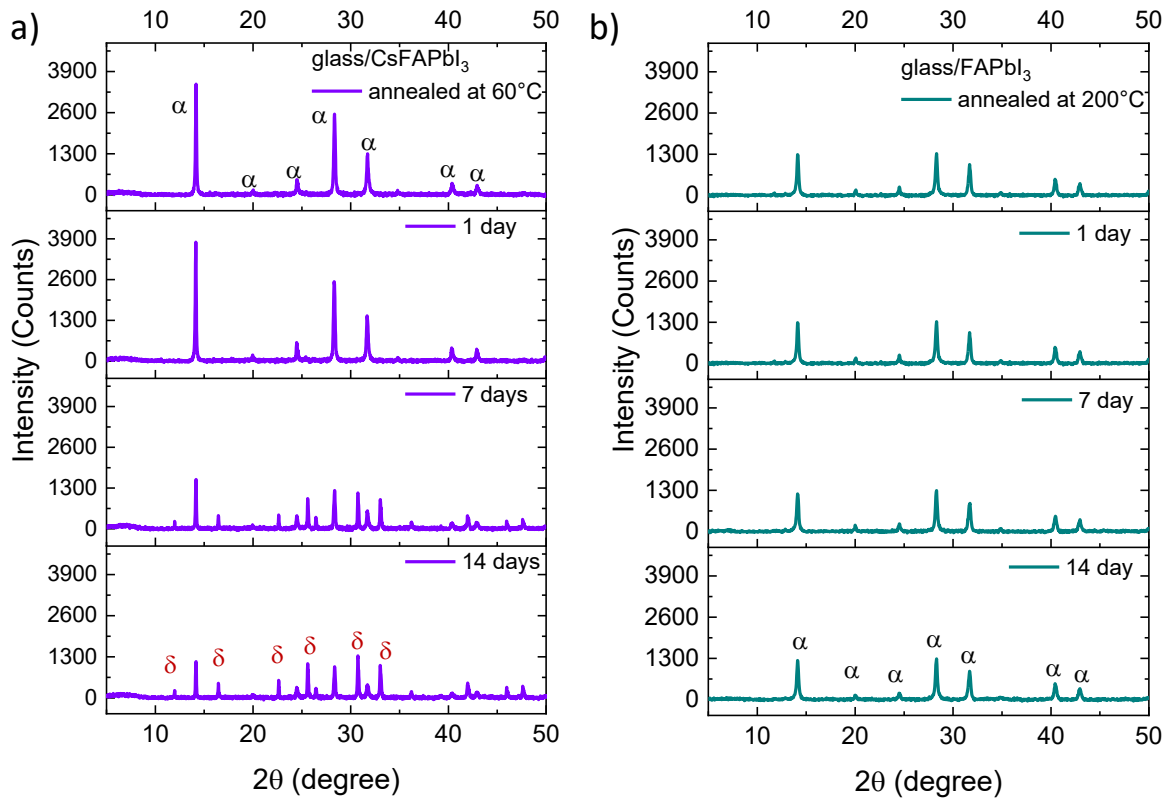
Figure 3. Storage stability of the perovskite layers. a,b) diffractograms over two weeks for a) CsFAPbI$_3$ and b) FAPbI$_3$ layers stored under dry air. Planes labeled in black correspond to α-phase and in brown to δ-phase.

2.1.3 Morphology and crystallization of thin films

The ultimate aim of the SSVD technique is to fabricate the PSCs on an industrial scale, and the compact placement of multilayers is very crucial for the interfacial issue. It has been widely reported that the chemical groups of underlayer influence the perovskite formation and stability,[37] we, therefore, investigated the formation of the perovskite layer on different organic materials. We extended our study to the state-of-the-art used underlayers. MoO$_3$/TaTm (TaTm= N4,N4,N4″,N4″-tetra([1,1′-biphenyl]-4-yl)-[1,1′:4′,1″-terphenyl]-4,4″-diamine), MoO$_3$/spiro-OMeTAD (N^2,N^2,N$^{2'}$,N$^{2'}$,N^7,N^7,N$^{7'}$,N$^{7'}$-octakis(4-methoxyphenyl)-9,9′ spirobi[9H-fluorene]-2,2′,7,7′-tetramine), c-TiO$_2$/SnO$_2$ and MeO-2PACz ([2-(3,6-dimethoxy-9*H*-carbazole-9-yl)-ethyl)phosphonic] acid. The underlayer chosen was of interest due to their different chemical nature and functional groups. TaTm has only benzene-groups, Spiro-OMeTAD methoxy-groups, MeO-2PACz phosphonic acid groups, and the inorganic oxide SnO$_2$, to have one reference that is not an organic one. TaTm[38], Spiro-OMeTAD[37], and MeO-2PACz[24] have been studied as underlayers in vacuum-deposited PSCs, and the

influence of functional groups was reported. Marcel Ross et al.[24] reported the impact of phosphonic groups in MeO-2PACz on the perovskite formation of FAPbI$_3$ during the MSVD process. We have described a positive effect MeO-groups on the perovskite crystallization, leading to micrometer-sized crystal features.[37]
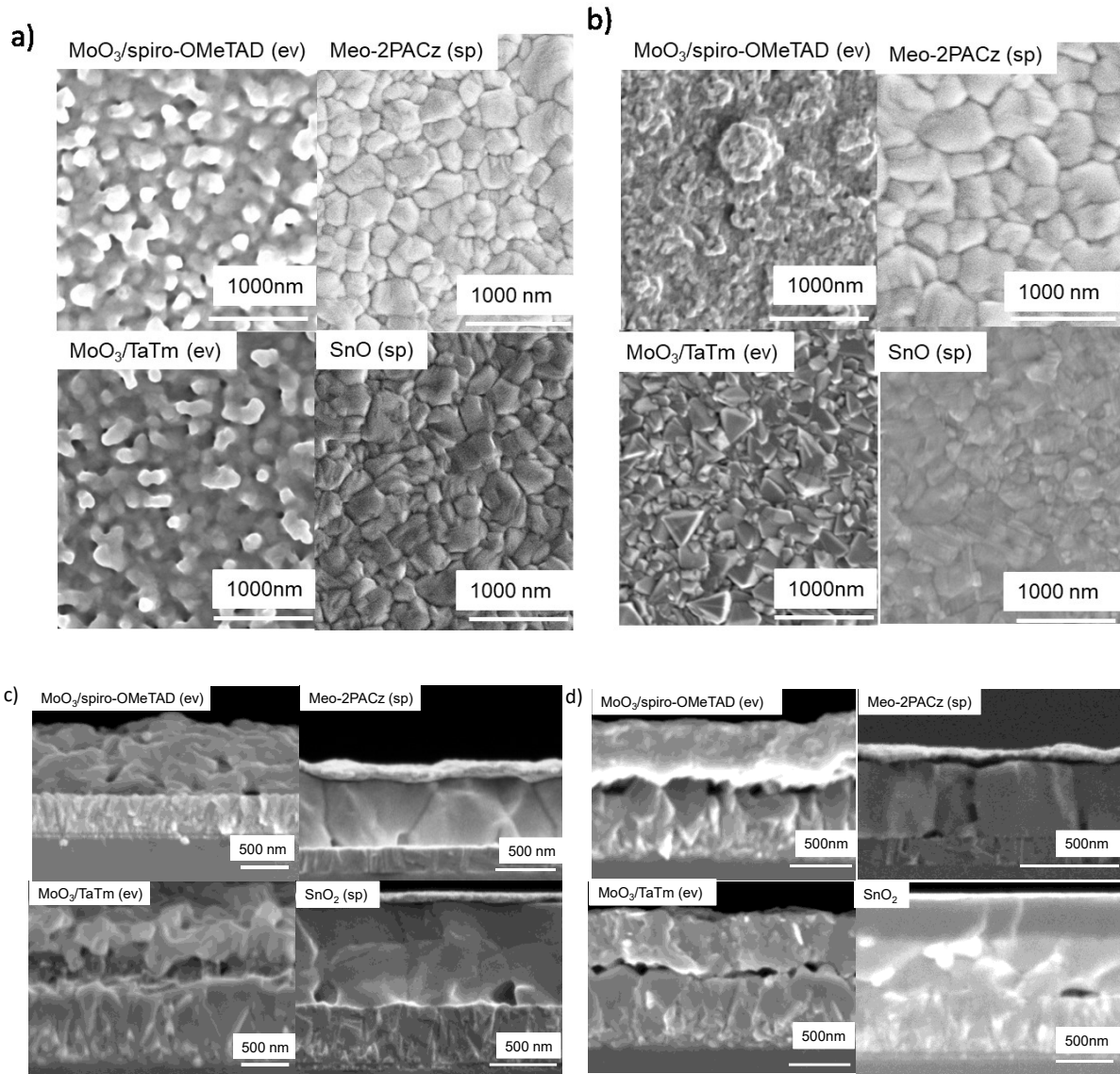

Figure 4: Top-view and cross section SEM images of annealed perovskite deposited on different underlayers a) α-CsFAPbI$_3$ (0.35 Å/s) b) α-FAPbI$_3$, (1.0-1.05 Å/s): (ev)=evaporated layer and (sp)=spin-coated layer deposited at 0.35Å/s c) cross-section SEM of α-CsFAPbI$_3$ (0.35 Å/s) d) cross-section SEM of α-FAPbI$_3$, (1.0-1.05 Å/s): (ev)=evaporated layer and (sp)=spin-coated layer deposited at 0.35Å/s.

Microstructure analysis was made by performing scanning electron microscopy (SEM). Top-view SEM images of the post-annealed α-CsFAPbI$_3$ and α-FAPbI$_3$ thin films deposited with the SSVD (Figure 4 a, b) reveal the formation of large perovskite crystals with a homogeneous coverage without pinholes for both types of perovskites. The α-CsFAPbI$_3$ reveal that agglomerates and a grain-like feature formed on top of the underlayer MoO3/Spiro-OMeTAD and MoO3/TaTm. Grain size distribution (Supporting Figure S13, S14) reveals that the perovskite formed on MoO$_3$/TaTm has larger grain sizes with an average grain size of ~358 nm than the grains on MoO$_3$/Spiro-OMeTAD (~333 nm). On SnO$_2$ and MeO-2PACz, the perovskite grains showed a larger average size (~455nm and ~404nm) and can be easily distinguished by their grain-like features. The top-view SEM images for α-FAPbI$_3$ show agglomerates of grain-like features for the perovskite on MoO$_3$/TaTm (~324 nm), while for MoO$_3$/Spiro-OMeTAD, pyramid-like grain features (~484 nm) appears. For the underlayer SnO$_2$ and MeO-2PACz, similar features can be observed for α-FAPbI$_3$ as for α-CsFAPbI$_3$, the grains formed with clear grain boundaries, indicating the larger grain sizes. Larger grains can be observed for the perovskite on SnO$_2$ (~530 nm) than for the perovskite on MeO-2PACz (~398 nm). By comparing the crystal size of α-CsFAPbI$_3$ with α-FAPbI$_3$ (excluding perovskite on top of MoO$_3$/TaTm due to unclear grain-like features), one can observe that the total crystal sizes are smaller for the α-CsFAPbI$_3$ than for α-FAPbI$_3$. This aligns with our hypothesis, where we noted a shift in XRD patterns towards higher angels on Cs incorporation into the crystal structures and higher crystallinity by an increase in intensity. Cs is known to reduce the grain sizes by increasing the density of crystal nuclei during the film formation, leading to reduced grain sizes and the absence of agglomerations.[39] The SEM cross-section images (Figure 4 c, d) for CsFAPbI$_3$ display that the perovskite layer is not well crystallized on the underlayers MoO$_3$/Spiro-OMeTAD and MoO$_3$/TaTm. On MeO-2PACz and SnO$_2$, the perovskite crystallization is improved, revealing large crystals (~450 nm for MeO-PACz and ~400 nm for SnO$_2$). However, pinholes are dominant at the interface. Similar observations are also inferred from the cross-section images for FAPbI$_3$. The perovskite layer generally shows an improved crystalline than CsFAPbI3, and the perovskite layers are not fully attached to the substrate, revealing either complete separation (MoO$_3$/Spiro-OMeTAD and MoO$_3$/TaTm) or pinholes (MeO-2PACz and SnO$_2$). Unfortunately, no typical perovskite crystallization was possible on MoO$_3$/TaTm and MoO$_3$/Spiro-OMeTAD, suggesting a negative effect of methoxy and benzene-groups on the perovskite crystallization when deposited by SSVD methods.

Interestingly, the cross-section images for both the perovskites reveal different layer thicknesses when considering the underlayers SnO_2 and MeO-2PACz, where the perovskite crystallized with large grains. We note that the samples with the same type of perovskite were fabricated during the same evaporation process; therefore, this change cannot be explained due to inconsistencies between the evaporation processes. Nevertheless, the cross-sectional images show significant deformity in the perovskite at the interface and reveal a difference in perovskite thickness when comparing the samples deposited on the metal oxide SnO_2 (~400 nm thickness) and the organic underlayer MeO-2PACz (~450 nm thickness). The interaction of the perovskite can explain this difference in the thickness with the underlayer as metal oxides are known to have a catalytic surface. Olthof *et al.* reported that a passivation layer of 30 nm of degradation products is deposited first until the perovskite formation can start.

On the other hand, the perovskite formation already starts after 3 nm of deposition for organic underlayers.[40] In earlier studies, we have found the influence of the underlayer on the co-evaporated methylammonium lead iodide perovskite formation. Oxides were significantly hindered due to their catalytic nature, promoting only after 100 nm precursor deposition perovskite growth.[37] In the case of the underlayer SnO_2, large holes can be observed independently of the perovskite deposited. Similar large holes are observed for the α-CsFAPbI$_3$ and α-FAPbI$_3$ films with the underlayer of MeO-2PACs. The perovskite layers are compact with large crystal sizes; however, further optimization of the SSVD process is necessary to prevent the formation of pinholes at the interface. However, our findings suggest the underlayer MeO-2PACz and SnO_2 are suited candidates to continue optimization for the implementation in *p-i-n* or *n-i-p* device structures.

3. Conclusion

In summary, we demonstrated successful employment of the SSVD technique to fabricate CsFAPbI$_3$ and FAPbI$_3$ thin films without the excess usage of FAI or CsI. PXRD, UV-Vis absorption, PL, and GIWAXS analyses were employed to confirm the high phase purity for the deposited films. We have additionally analyzed the feasibility of device fabrication from these layers and established that impairment of the perovskite could be seen on all of the state-of-the-art underlayers except on SnO_2 and MeO-2PACz. These findings suggest that an optimization of the composition of the perovskite powder is crucial when following up on the single-source evaporation as an upgraded technique towards large-scale application in the future.

4. Experimental Section

Materials:

All chemicals were purchased from Sigma Aldrich and were used as received without further purification unless otherwise stated.

Perovskite powder synthesis:

The δ-FAPbI$_3$ powder was synthesized through a previously reported room temperature precipitation method1 where 2.675 mmol FAI (synthesized from formamidine acetate1) was dissolved in 30 ml of acetonitrile (HPLC grade, Alfa Aeser) by stirring. 2.075 mmol of PbI2 (99%) was added to the stirring solution and continued the stirring for another 24 hours. The yellow powders were filtered, and the residual PbI$_2$ and FAI were removed by five-time washing with acetonitrile solvent followed by a one-time wash with diethyl ether. Roto-evaporator was used to remove the solvents, and vacuum dried powder was used for further characterizations.

The α-CsFAPbI$_3$ powder was synthesized by annealing the previously reported δ-CsFAPbI$_3$ powder in a tube furnace at 150 °C for 1 hour under an N$_2$ atmosphere. Then obtained α-CsFAPbI$_3$ powder was transferred to a clean vial and kept in the glovebox until use.

Underlayer preparation

Thin films were fabricated on fluorine-doped tin oxide (FTO)-coated glass substrates (TEC-15AX, NSG group) previously cleaned by a sequential sonication treatment in a 2% Hellmanex solution, acetone, and isopropanol, followed by ultraviolet–ozone treatment for 15 min. A compact blocking layer of TiO$_2$ (planar-TiO$_2$, 30 nm thick film) was then deposited onto the FTO-coated glass substrate by spray pyrolysis, using a titanium diisopropoxide bis(acetylacetonate) (TAA) solution (Sigma-Aldrich) in ethanol (1ml of TAA in 15ml ethanol), and then sintered at 450 °C for 30 min. Then, a 20 nm SnO$_2$ was prepared by dissolving SnCl$_4$ (Acros) in deionized water (12 μl in 988 μl water). This solution was spin-coated at 3000 rpm for 30 s (1000 rpm/s acceleration) on top of the meso-TiO$_2$. After annealing at 190 °C for 1h a 20 nm thick layer was formed. The MeO-2PACz solution was prepared, weighing 1.5g into ethanol. The solution was sonicated for 15min. Then the solution was ITO substrates, which were cleaned 10min additionally in the oxygen plasma before the solution was spin-coated in a nitrogen-filled glovebox. The solution was spin-coated at 4000 rpm for 35s and directly

annealed for 10 min at 100°C. MoO3, TaTm, spiro-OMeTAD, C_{60} BCP were evaporated in a PRO Line PVD 75 vacuum chamber from Kurt J. Lesker Company equipped with four thermally controlled sources. 5nm MoO_3 was evaporated at a rate of 0.1 Å/s at a 76 A, the 10nm spiro-OMeTAD was prepared at a rate of 0.5 Å/s at ~290°C, 10nm TaTm was evaporated at a rate of 0.1 Å/s at ~295-300°C.

The prepared layers were transferred to the PRO Line PVD 75 vacuum chamber from Kurt J. Lesker Company equipped with four thermally controlled sources. The crucibles were filled with the perovskite precursors and power was applied to sublime the perovskite powders. $CsFAPbI_3$ perovskite powder was evaporated at 0.35Å/s (16.2% power) and $FAPbI_3$ was evaporated at a rate of 1.0-1.5 Å/s (16.2%) during a vacuum pressure of ~$1 \cdot 10^{-6}$ mbar. During perovskite deposition, the deposition rate of each precursor was kept constant and monitored by independent quartz microbalance crystal sensors (QCMs). The substrates were kept at room temperature and under rotation of 5 r.p.m.

Materials Characterizations:

The XRD patterns of the prepared films were measured using a D8 Advance diffractometer from Bruker (Bragg-Brentano geometry, with an X-ray tube Cu Kα, λ = 1.5406 Å). Steady-state photoluminescence (PL) measurements were recorded with an LS-55 fluorescence spectrometer (PerkinElmer, Inc.), at an excitation wavelength λ = 450 nm. TrPL was measured with a Fluorolog TCSPC (HORIBA, Ltd.) was used to measure time-resolved photoluminescence (TRPL) with 760nm as the detection wavelength.

X-ray scattering (2D-WAXS) patterns represented in reciprocal lattice space were performed at SPring-8 on beamline BL19B2. The samples were irradiated with an X-ray energy of 12.39 keV (λ = 1 Å) at a fixed incident angle on the order of 0.12°through through a Huber diffractometer. The 2D-WAXS patterns were measured with a two-dimensional image detector (Pilatus 300K). The X-ray photoelectron spectroscopy (XPS) measurements were carried out on a VersaProbe II (Physical Electronics, Inc.) with a monochromatic Al K_α X-ray source operating at 1486.6 eV. The spectra were referenced using the Pb 4f signal. Data were processed using CasaXPS.

A FEI Teneo Schottky Field Emission SEM was used for recording the scanning electron microscopy (SEM) images by an in-lens detector of at tension of 1.5 kV for top-view imaging and 1 kV for cross-section analysis.

The thermogravimetric measurements were done in a TGA 4000 from PerkinElmer. In the tared crucibles (N5200040) 2-15mg of sample were added. Then under nitrogen athmosphere, 1 min isotherm at 30°C, then heating up to 700°C at a rate of 10°C/min, and 1min isotherm at 700°C for FAPbI$_3$ and the same but until higher temperature (1 min isotherm at 900°C) for CsFAPbI$_3$.

Supporting Information
Supporting Information is available from the Wiley Online Library or the author.

Corresponding Author

Author Contributions

References

[1]   A. Kojima, K. Teshima, Y. Shirai, T. Miyasaka, *J. Am. Chem. Soc.* **2009**, *131*, 6050.

[2]   NREL Research Cell Record Efficiency Chart, **2021**.

[3]   K. P. Goetz, A. D. Taylor, Y. J. Hofstetter, Y. Vaynzof, *ACS Appl. Mater. Interfaces* **2021**, *13*, 1.

[4]   M. Cai, Y. Wu, H. Chen, X. Yang, Y. Qiang, L. Han, *Adv. Sci.* **2017**, *4*.

[5]   A. Binek, M. L. Petrus, N. Huber, H. Bristow, Y. Hu, T. Bein, P. Docampo, *ACS Appl. Mater. Interfaces* **2016**, *8*, 12881.

[6]   K. P. Goetz, A. D. Taylor, Y. J. Hofstetter, Y. Vaynzof, *ACS Appl. Mater. Interfaces* **2021**, *13*, 1.

[7]   G. Divitini, S. Cacovich, F. Matteocci, L. Cinà, A. Di Carlo, C. Ducati, *Nat. Energy* **2016**, *1*, 15012.

[8]   Y. Han, S. Meyer, Y. Dkhissi, K. Weber, J. M. Pringle, U. Bach, L. Spiccia, Y. B. Cheng, *J. Mater. Chem. A* **2015**, *3*, 8139.

[9]   N. Aristidou, I. Sanchez-Molina, T. Chotchuangchutchaval, M. Brown, L. Martinez, T. Rath, S. A. Haque, *Angew. Chemie - Int. Ed.* **2015**, *54*, 8208.

[10]   K. Wojciechowski, T. Leijtens, S. Siprova, C. Schlueter, M. T. Hörantner, J. T. W. Wang, C. Z. Li, A. K. Y. Jen, T. L. Lee, H. J. Snaith, *J. Phys. Chem. Lett.* **2015**, *6*, 2399.

[11]   G. E. Eperon, S. D. Stranks, C. Menelaou, M. B. Johnston, L. M. Herz, H. J. Snaith, *Energy Environ. Sci.* **2014**, *7*, 982.

[12]   T. Liu, Y. Zong, Y. Zhou, M. Yang, Z. Li, O. S. Game, K. Zhu, R. Zhu, Q. Gong, N. P. Padture, *Chem. Mater.* **2017**, *29*, 3246.

[13]   M. Saliba, T. Matsui, K. Domanski, J. Y. Seo, A. Ummadisingu, S. M. Zakeeruddin, J. P. Correa-Baena, W. R. Tress, A. Abate, A. Hagfeldt, M. Grätzel, *Science (80-.).* **2016**, *354*, 206.

[14]   N. Leupold, F. Panzer, *Adv. Funct. Mater.* **2021**, *31*.

[15]   J. Ávila, C. Momblona, P. P. Boix, M. Sessolo, H. J. Bolink, *Joule* **2017**, *1*, 431.

[16]   P. Fan, D. Gu, G. X. Liang, J. T. Luo, J. L. Chen, Z. H. Zheng, D. P. Zhang, *Sci. Rep.* **2016**, *6*, 1.

[17]   R. Vidal, J. A. Alberola-Borràs, S. N. Habisreutinger, J. L. Gimeno-Molina, D. T. Moore, T. H. Schloemer, I. Mora-Seró, J. J. Berry, J. M. Luther, *Nat. Sustain.* **2021**, *4*, 277.

[18]   N. G. Park, *Nat. Sustain.* **2021**, *4*, 192.

[19]   B. Dänekamp, C. Müller, M. Sendner, P. P. Boix, M. Sessolo, R. Lovrincic, H. J. Bolink, *J. Phys. Chem. Lett.* **2018**, *9*, 2770.

[20]   J. Borchert, R. L. Milot, J. B. Patel, C. L. Davies, A. D. Wright, L. Martínez Maestro, H. J. Snaith, L. M. Herz, M. B. Johnston, *ACS Energy Lett.* **2017**, *2*, 2799.

[21]   L. Gil-Escrig, C. Dreessen, I. C. Kaya, B. S. Kim, F. Palazon, M. Sessolo, H. J. Bolink, *ACS Energy Lett.* **2020**, *5*, 3053.

[22]   Y. H. Chiang, M. Anaya, S. D. Stranks, *ACS Energy Lett.* **2020**, *5*, 2498.

[23]   L. Gil-Escrig, C. Dreessen, F. Palazon, Z. Hawash, E. Moons, S. Albrecht, M. Sessolo, H. J. Bolink, *ACS Energy Lett.* **2021**, *6*, 827.

[24]   M. Roß, S. Severin, M. B. Stutz, P. Wagner, H. Köbler, M. Favin-Lévêque, A. Al-Ashouri, P. Korb, P. Tockhorn, A. Abate, B. Stannowski, B. Rech, S. Albrecht, *Adv. Energy Mater.* **2021**, *11*.

[25]   M. J. Crane, D. M. Kroupa, J. Y. Roh, R. T. Anderson, M. D. Smith, D. R. Gamelin, *ACS Appl. Energy Mater.* **2019**, *2*, 4560.

[26]   Y. El Ajjouri, F. Palazon, M. Sessolo, H. J. Bolink, *Chem. Mater.* **2018**, *30*, 7423.

[27]   M. P. U. Haris, S. Kazim, S. Ahmad, *ACS Appl. Energy Mater.* **2021**, *4*, 2600.

[28]   D. B. Straus, S. Guo, R. J. Cava, *J. Am. Chem. Soc.* **2019**, *141*, 11435.

[29]   B. Slimi, M. Mollar, I. Ben Assaker, A. Kriaa, R. Chtourou, B. Marí, *Monatshefte fur Chemie* **2017**, *148*, 835.

[30]   P. Luo, W. Xia, S. Zhou, L. Sun, J. Cheng, C. Xu, Y. Lu, *J. Phys. Chem. Lett.* **2016**, *7*, 3603.

[31]   D. Shi, V. Adinolfi, R. Comin, M. Yuan, E. Alarousu, A. Buin, Y. Chen, S. Hoogland, A. Rothenberger, K. Katsiev, Y. Losovyj, X. Zhang, P. A. Dowben, O. F. Mohammed, E. H. Sargent, O. M. Bakr, *Science (80-.).* **2015**, *347*, 519.

[32]   Y. Yang, Y. Yan, M. Yang, S. Choi, K. Zhu, J. M. Luther, M. C. Beard, *Nat. Commun.* **2015**, *6*.

[33]   Y. Zhang, S. G. Kim, D. Lee, H. Shin, N. G. Park, *Energy Environ. Sci.* **2019**, *12*, 308.

[34]   J. B. Patel, R. L. Milot, A. D. Wright, L. M. Herz, M. B. Johnston, *J. Phys. Chem. Lett.* **2016**, *7*, 96.

[35]   Z. Li, M. Yang, J. S. Park, S. H. Wei, J. J. Berry, K. Zhu, *Chem. Mater.* **2016**, *28*, 284.

[36]   N. Li, Z. Zhu, C. C. Chueh, H. Liu, B. Peng, A. Petrone, X. Li, L. Wang, A. K. Y. Jen, *Adv. Energy Mater.* **2017**, *7*.

[37]   N. Klipfel, C. Momblona, H. Kanda, N. Shibayama, Y. Nakamura, M. D. Mensi, C. Liu, C. Roldán-Carmona, M. K. Nazeeruddin, *Sol. RRL* **2021**, 2100191.

[38] C. Momblona, L. Gil-Escrig, E. Bandiello, E. M. Hutter, M. Sessolo, K. Lederer, J. Blochwitz-Nimoth, H. J. Bolink, *Energy Environ. Sci.* **2016**, *9*, 3456.

[39] Y. Yu, C. Wang, C. R. Grice, N. Shrestha, J. Chen, D. Zhao, W. Liao, A. J. Cimaroli, P. J. Roland, R. J. Ellingson, Y. Yan, *ChemSusChem* **2016**, *9*, 3288.

[40] S. Olthof, K. Meerholz, *Sci. Rep.* **2017**, *7*, 1.